Chinese Chemical Letters 37 (2026) 111529

Contents lists available at ScienceDirect

Chinese Chemical Letters

journal homepage: www.elsevier.com/locate/cclet

Crystallization-induced emission enhancement of copper iodide cluster for efficient X–ray scintillation and dynamic imaging

Hao-Nan Qin, Hao Xie, Jia-Wang Yuan, Ren-Wu Huang*, Zhao-Yang Wang*, Shuang-Quan Zang

Henan Key Laboratory of Crystalline Molecular Functional Materials, Henan International Joint Laboratory of Tumor Theranostical Cluster Materials, Green Catalysis Center and College of Chemistry, Zhengzhou University, Zhengzhou 450001, China

ARTICLE INFO

Article history:
Received 29 March 2025
Revised 26 June 2025
Accepted 2 July 2025
Available online 3 July 2025

Keywords:
Copper iodide cluster
Crystallization-induced emission
Radioluminescence
Scintillation
X–ray scintillation imaging

ABSTRACT

Zero-dimensional (0D) scintillation materials have demonstrated great potential in X-ray detection and imaging due to their advantages in fabricating flexible screens. Compared with the current lead-halide perovskite-based nanocrystals and quantum dots, copper iodide clusters have gradually attracted attention due to their better air stability, eco-friendliness, and processability performance. Here, we demonstrate large-scale synthesis of an eco-friendly 0D microcrystalline $Cu_4I_6(DABCO–CH_3)_2$ (Cu_4I_6, $DABCO–CH_3$ = 1-methyl-4-aza-1-azoniabicyclo[2.2.2]octane) scintillator exhibiting crystallization-induced emission enhancement (CIEE). High X-ray absorption efficiency and excellent optical properties endow Cu_4I_6 microcrystals with high-quality scintillation performance, which displays an ultralow X-ray detection limit of 38.4 nGy/s and a light yield of ~21,700 photons/MeV. Specifically, a microcrystal-based flexible scintillation screen was fabricated for high-resolution static and dynamic X-ray imaging applications, achieving a spatial resolution of 12.3 LP/mm. This study introduces a practical design concept for CIEE-based scintillators and seeks to further investigate their potential applications in X-ray imaging.

© 2026 Published by Elsevier B.V. on behalf of Chinese Chemical Society and Institute of Materia Medica, Chinese Academy of Medical Sciences.

Scintillators have drawn tremendous attention for their ability to convert high-energy radiation into low-energy UV–vis light, showing their great potential in security inspection, biomedicine, and astrophysics [1–6]. At present, traditional inorganic scintillators (CsI:Tl, CaF_2:Eu, $PbWO_4$, $Bi_4Ge_3O_{12}$, *etc.*) have been successfully commercialized due to the advantages of excellent absorption coefficient and high light yield [7–12]. However, harsh preparation conditions, such as high processing temperatures and complicated preparation processes, increase the production cycle and costs, and seriously hinder their use in the development of novel flexible X-ray imaging [13–17]. Moreover, certain inorganic scintillators demonstrate significant susceptibility to moisture-induced degradation, posing additional challenges for long-term device storage [18–23]. The development of scintillator materials with excellent processability, cost-effectiveness, and high performance holds immense scientific and practical importance for advancing various fields.

Recently, zero-dimensional (0D) scintillator materials including the lead-halide perovskite-based nanocrystals and quantum dots have been applied in large-scale scintillation screens for X-ray imaging due to their outstanding solution processability [24–29]. However, the photon self-absorption effect that severely leads to aggregation-caused luminescence attenuation and inherently highly toxic metal Pb may both be crucial reasons to limit their commercial applications [30–34]. To overcome the agglomeration, the addition of surfactants (such as PVP) is an efficient synthetic strategy for the formation of homogeneous nano or microcrystal scintillators [35–39]. Inspired by the unique optical behavior of crystallization-induced emission enhancement [40–42], we envision that this property can effectively prevent scintillators from aggregation-caused luminescence attenuation, in addition, the nano and micro-scale crystals with excellent optical properties can be prepared under mild conditions for the preparation of flexible scintillation screen. Currently, copper iodide clusters emerge as a new class of eco-friendly X-ray scintillators due to their rich structural diversity and excellent photophysical properties, such as exceptional X-ray absorption capability and high PLQY [43–46]. In addition, the unique cluster-centered emission makes Cu(I)-I clusters exhibit a shorter decay time in comparison to the MLCT/XMCT photoluminescence of common Cu(I)-based complexes reported, further demonstrating the great potential for dynamic X-ray imaging applications [47,48].

* Corresponding authors.
E-mail addresses: renwuhuang@zzu.edu.cn (R.-W. Huang), wangzy@zzu.edu.cn (Z.-Y. Wang).

https://doi.org/10.1016/j.cclet.2025.111529
1001-8417/© 2026 Published by Elsevier B.V. on behalf of Chinese Chemical Society and Institute of Materia Medica, Chinese Academy of Medical Sciences.

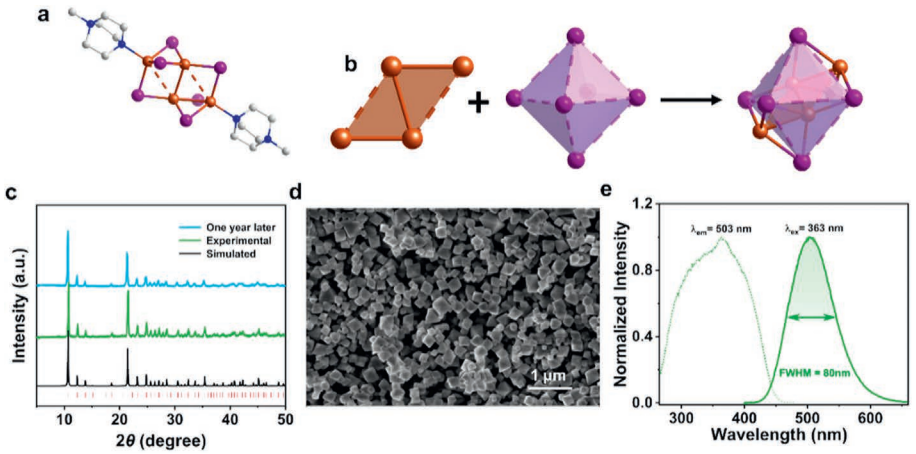


Fig. 1. (a) Total atomic structure of $Cu_4I_6(DABCO–CH_3)_4$. Color legend: Cu, brown; I, purple; C, gray; N, bule. (b) *Quasi*-rhombic geometry of the tetranuclear Cu_4 kernel and I_6 octahedral shell. (c) Powder X-ray diffraction (PXRD) patterns of Cu_4I_6 microcrystal. (d) SEM image of Cu_4I_6 microcrystal. (e) PL spectra of Cu_4I_6 at room temperature.

In this work, we synthesized a uniformly sized 0D Cu_4I_6 microcrystalline scintillator by a simple solution protocol on a large scale at room temperature, which shows crystallization-induced emission enhancement property. The water oxygen stable Cu_4I_6 microcrystals display a narrow emission band at 503 nm with a PLQY up to 61.23 %. The unique optical properties and heavy X-ray absorption ability endow Cu_4I_6 microcrystals high-quality radioluminescence (RL) performance, with an ultralow X-ray detection limit of 38.4 nGy/s, a high scintillator light yield of 21,700 photons/MeV, and a high resistance to radiation. More importantly, due to the highly dispersed microcrystalline morphology and low economic cost of Cu_4I_6, large-area (up to 100 cm^2) and flexible X-ray scintillator screens were fabricated for high-quality, sensitive static and dynamic X-ray imaging applications of large-volume objects with a high resolution of 12.3 LP/mm. This work suggests that those CIEE-active copper iodide clusters hold great promise in high-energy detection and X-ray imaging applications.

The high-quality crystals of $Cu_4I_6(DABCO–CH_3)_2$ were obtained by the liquid phase diffusion method at room temperature. Briefly, the ethanol solution of $DABCO–CH_3$ was slowly added to a solution of CuI in acetonitrile and dichloromethane. Then, the resulting clear solution was allowed to evaporate in a dark environment at 4 °C to afford crystals of Cu_4I_6 for X-ray diffraction. In contrast to the conventional synthesis of microcrystals, the Cu_4I_6 microcrystals were synthesized by a simple, eco-friendly, and low-cost solution method, in absence of toxic surfactants such as polyvinyl pyrrolidone (PVP). CuI and $DABCO–CH_3$ powders with a molar ratio of 2:1 were dissolved in fresh acetonitrile and ethanol solution, respectively, to form a transparent solution at room temperature. The CuI in acetonitrile was poured into the ethanol solution of $DABCO–CH_3$ to immediately produce a large amount of Cu_4I_6 microcrystals with a high yield of ~95 % (Fig. S1 in Supporting information). The detailed experimental procedure can be seen in Supporting information. This method of synthesizing Cu_4I_6 clusters at the gram-scale under mild conditions has offered substantial benefits for the fabrication of large-sized scintillator screens.

SCXRD analysis revealed that Cu_4I_6 crystallizes in the cubic space group $Pa\bar{3}$ and consists of four Cu atoms, six I atoms, and two $DABCO–CH_3$ ligands in each cluster (Fig. 1a). The overall structure shows an I_6 octahedron being halved crosswise by an Cu_4 parallelogram (Fig. 1b), and the $DABCO–CH_3$ ligands coordinated to the exposed Cu atoms. The packing diagrams shown in Fig. S2 (Supporting information) display that Cu_4I_6 self-assembles into a hexagonal closest packing (HCP) pattern with perfect face-to-face contact of neighboring Cu_4I_6 and interdigitation of intercluster surface ligands.

The crystalline phase purity of the gram-scale synthesized Cu_4I_6 powder was confirmed by powder X-ray diffraction (PXRD) (Fig. 1c). Meanwhile, the scanning electron microscopy (SEM) image of Cu_4I_6 exhibited a uniform size distribution of microcrystals with rhombic block morphology (Fig. 1d), which is beneficial to forming a dense and uniform scintillator screen. Furthermore, the Cu_4I_6 microcrystals can maintain stability until approximately 280 °C, as revealed by the thermogravimetric analysis (Fig. S3 in Supporting information), manifesting a significantly good thermal stability.

The photophysical performance of the fresh Cu_4I_6 crystals was studied by UV–vis absorption and PL spectra. The UV–vis absorption spectra of Cu_4I_6 displayed optical bandgaps of 2.99 eV (Fig. S4 in Supporting information), and the low bandgap favors better RL [48]. Fig. 1e shows the PL and PL excitation (PLE) spectra of Cu_4I_6, which exhibit intense color-pure green emission centered at 503 nm with a full width at half-maximum (FWHM) of 80 nm under UV-light excitation. The large Stokes shift (140 nm) and corresponding microsecond scale lifetime (3.59 μs) indicate the phosphorescence nature (Fig. S5 in Supporting information). Moreover, a high PLQY of 61.23 % was acquired by adopting an absolute PL measurement system (Fig. S6 in Supporting information). It is worth noting that the large Stokes shift and high PLQY are beneficial for obtaining a decent scintillation light yield. It is noted that the structure of metal clusters has a significant effect on optical properties. For instance, the Cu_4I_6 clusters with identical core but different organic cation ligands have been reported previously, but exhibiting several PLQY and emission wavelengths [35,38]. Meanwhile, the Xia's group reported the influence of different halide anion on scintillator performance of two copper(I)-based clusters Cu_3X_3 (X = Cl, Br). They have considered that Cu_3Br_3 cluster with low halogen electronegativity further weakened halogen-to-ligand charge transfer (XLCT) emission, enabling enhanced quantum efficiency and scintillation performance than that of the chloride one [47]. Furthermore, the crystal size of metal clusters directly affects their electronic structure, especially the quantization degree of the energy level spacing. When the cluster size is reduced to the nanometer level, the quantum size effect causes its electronic energy level to change from a continuous state to a discrete state, thereby affecting the light absorption and emission characteristics [50]. Density functional theory (DFT) computation was conducted to understand the PL mechanism of Cu_4I_6. The electron densities of HOMO and LUMO were mainly localized in the regions surrounding the Cu/I atoms and the planar tetranuclear copper structure, respectively, indicating a cluster centered (CC) electronic transitions (Fig. S7 in Supporting information) [47].

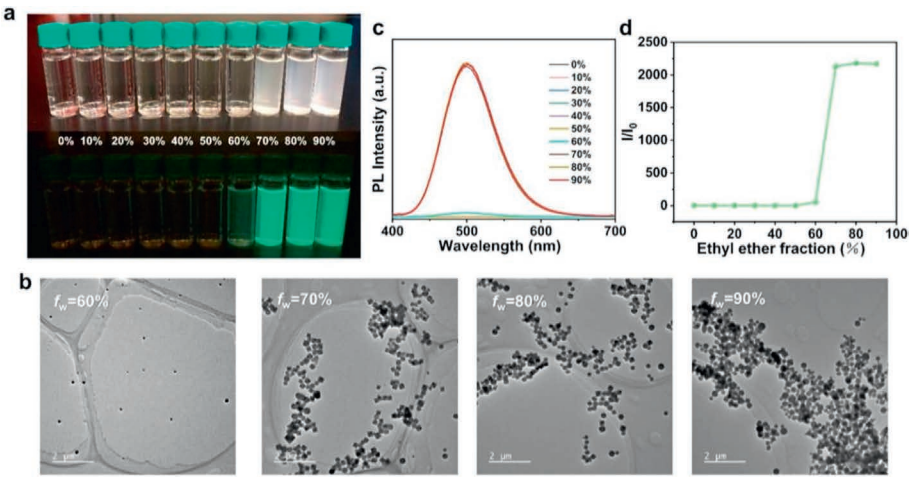


Fig. 2. (a) Photographs of Cu_4I_6 in mixed solvents with $f_w = 0–90\%$ (Et_2O/CH_3CN) under ambient light (top) and UV light (bottom). (b) TEM images of Cu_4I_6-assembled microcrystal at $f_w = 60\%$, 70%, 80%, and 90%. (c) PL spectra of Cu_4I_6 in mixed solvents with different f_w values. (d) Plot of the relative PL intensity (I/I_0) of Cu_4I_6 in mixed solvents as a function of f_w, where I_0 and I are the maximum PL intensities in a CH_3CN solution and a Et_2O/CH_3CN solution.

In nanomaterials, AIEE or CIEE is a photophysical phenomenon that receives wide attention, in which luminophores experience a rise in PL efficiency with their self-assembly and aggregation than in dilute solution. As the solution of Cu_4I_6 in MeCN is non-emissive, the intense solid-state emission may be attributed to the AIE and CIE effects. Therefore, the CIEE activities of Cu_4I_6 were systematically analyzed in a MeCN/Et_2O solvent system.

As shown in Fig. 2a, the non-emissive transparent solution of Cu_4I_6 turned slightly cloudy when f_w ($f_w = vol_{Et_2O}/vol_{MeCN+Et_2O}$) was increased to 60% and exhibited a weak green emission under UV light. As f_w continued to increase from 60% to 70%, the PL intensity of the solution was sharply elevated (Figs. 2a and c). The PL intensity at $f_w = 70\%$ has risen >2200-fold ($I_{70\%}/I_0 = 2223$) in comparison to the pure MeCN solution of Cu_4I_6, with a high PLQY of 22.3%. Of note, the current microcrystal size is larger than that at $f_w = 60\%$ (Fig. 2a), which is similar to aggregate expansion in the AIE effect. Despite the microcrystals' quantity steadily increasing and size gradually aggregating as f_w increased from 70% to 90%, the PL intensity showed no significant change (Figs. 2c and d). In addition, the emission centered at 503 nm shows no obvious shift as the f_w increases (Fig. S8 in Supporting information), suggesting that the emission originates from the Cu_4I_6 microcrystals, which could be directly observed by transmission electron microscopy (TEM) images (Fig. 2b). Moreover, we found that there is a remarkable change in PLQY between the aggregated and crystal states of Cu_4I_6 (Fig. S9 in Supporting information), which can be attributed to defect-rich surfaces and low crystallinity induced by rapid crystallization in Et_2O solvents [51,52]. This phenomenon further proves the CIEE behavior of Cu_4I_6. Of note, this CIEE-active copper iodide clusters may effectively prevent clusters from aggregation-caused luminescence attenuation and further improving X-ray imaging ability.

Meanwhile, the dynamic light scattering (DLS) measurement reveals that the size of the aggregates increased with an increasing fraction of poor solvent (f_w: from 60% to 90%) (Fig. S10 in Supporting information). Finally, to verify the arrangement of Cu_4I_6 in aggregates, the aggregate particles ($f_w = 70\%$) were collected for high-resolution TEM and selected area electron diffraction (SAED) experiments (Fig. S11 in Supporting information), and the diffuse rings in the SAED pattern indicate the crystalline state of Cu_4I_6.

The large-scale production of low-cost high-quality Cu_4I_6 microcrystals exhibiting excellent optical properties makes them promising candidates for X-ray imaging applications. Thus, the RL properties of Cu_4I_6, including the light yield, detection limit, and antiradiation stability under X-ray irradiation, were systematically examined. According to the XCOM web database, we calculated the attenuation coefficient of Cu_4I_6, which is lower than the commercial scintillator BGO but higher than the reported Cu_4I_4Py scintillator (Fig. 3a), because of the presence of two extra I atoms with high X-ray absorption cross sections [45]. The relationship between the X-ray attenuation efficiencies and the thickness of the Cu_4I_6 scintillators over the entire range of X-ray photon energies has been investigated, and a 0.5 mm-thick Cu_4I_6 scintillator could absorb ≈ 83.24% of the incident X-rays (Fig. S12 in Supporting information). Furthermore, the X-ray attenuation efficiencies as a function of photon energy at a thickness of 0.5 mm were studied (Fig. 3b). Taking a commercially available BGO (LY: 8000–10,000 photons/MeV) as the reference, the light yield of Cu_4I_6 scintillator was measured to be 16,814–21,700 photons/MeV by comparing the integrated area of the RL spectra (Fig. 3c). The minimum detection limit is closely related to the sensitivity of scintillators to X-rays, as an important parameter of the practical applications of scintillators. As shown in Fig. 3d and Fig. S13 (Supporting information), the RL intensity of the Cu_4I_6 scintillator showed a linear dependence on the X-ray dose rate. Of note, based on a three-time signal-to-noise ratio (SNR), the detection limit of the Cu_4I_6 scintillator is calculated to be 38.4 nGy/s, which is about 143 times lower than the dose of 5.5 μGy/s for the medical treatment requirement of X-ray diagnostics. Additionally, the radiation stability of the Cu_4I_6 scintillator was examined under cyclical X-ray irradiation, as shown in Fig. 3e, the RL intensity of the Cu_4I_6 scintillator barely changed under a high X-ray dose (278 μGy/s) for one hour. The result indicated that the Cu_4I_6 scintillator demonstrated excellent X-ray radiation stability, which provides a feasible opportunity for X-ray imaging. Fig. 3f and Table S1 (Supporting information) show the preliminary cost analysis of the Cu_4I_6 scintillator and a comparison with other commercial or reported scintillators, and our scintillator is highly cost-effective [53]. Besides, the light yield of Cu_4I_6 is comparable to that of those scintillators mentioned above (Fig. S14 in Supporting information). All these findings fully convince that Cu_4I_6 is a candidate material for X-ray imaging. The PL and RL spectra of the Cu_4I_6 crystals at room temperature are almost identical with a negligible difference in emission center, implying that the emission likely originated from the same excited states (Fig. S15 in Supporting information).

The X-ray scintillation mechanism was further investigated. For the 0D Cu_4I_6 cluster-base scintillator, X-ray-excited luminescence mainly goes through the following processes (Fig. 3g). Under the

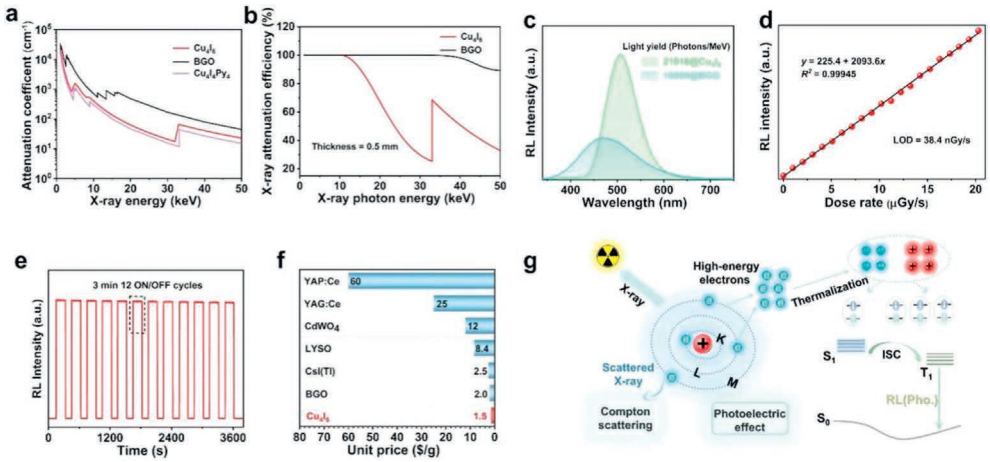


Fig. 3. (a) Plots of attenuation coefficient as a function of photon energy for Cu_4I_6, $Bi_4Ge_3O_{12}$ (BGO) and Cu_4I_4Py, from 1 keV to 50 keV. (b) Spectra of calculated X-ray attenuation efficiency as a function of X-ray photon energy at a thickness of 0.5 mm for Cu_4I_6 and reference BGO. (c) RL spectra of Cu_4I_6 and BGO wafers with the same thickness and sectional area. (d) Plot of RL intensity as a function of dose rates. The limit of detection (LOD) is defined as the X-ray dose rate required to produce a signal greater than three times the noise level and was derived from the fitting line where the signal-to-noise ratio equals 3. (e) Fatigue resistance of Cu_4I_6 under X-ray excitation (X-ray dose: 278 μGy/s). (f) Cost/price comparison of Cu_4I_6 and some other commercially available scintillators. (g) Schematic diagram of the scintillation process.

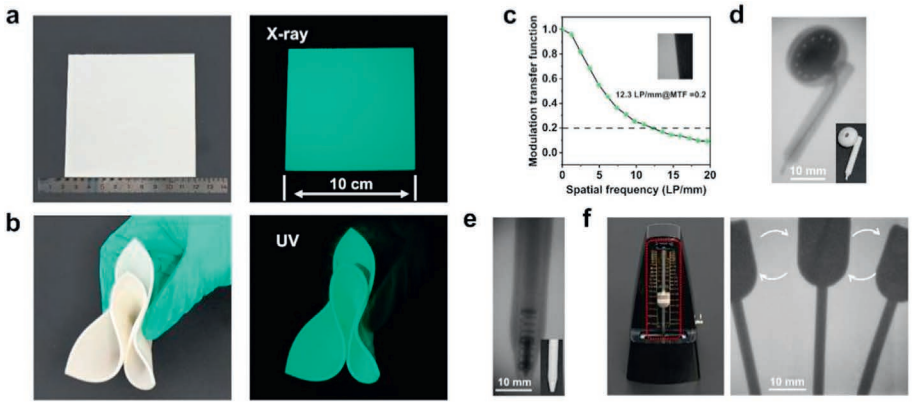


Fig. 4. Large-area and flexible X-ray scintillator screen. (a, b) Photographic image and luminescence image under UV and X-ray, respectively. (c) Modulation transfer functions (MTF) of X-ray images based on Cu_4I_6 scintillator. (d, e) X-ray images of wired in-ear headphone and ballpoint pen. (f) Imaging photographs of piano metronome display.

excitation of high-energy X-ray, the heavy atoms in the Cu_4I_6 scintillator interact with the X-ray photons through the photoelectric effect and Compton scattering, where the high-energy electrons escape from the inner shells of the atoms. Such high-energy electrons subsequently induce plentiful secondary electrons by colliding with atoms. Then these secondary electrons and holes quickly thermally relax to the lowest unoccupied molecular orbital (LUMO) and the highest occupied molecular orbital (HOMO) of the Cu_4I_6 cluster, forming the recombination of electron-hole pairs, and the singlet (S_n) and triplet (T_n) excitons are generated with a 1:3 ratio due to the exciton spin statistics. Finally, the triplet excitons (T_1) decay to the ground state (S_0) through a radiative transition process, generating intense phosphorescence emission. Besides, the calculations of the excited states could offer a more profound understanding of the phosphorescence transition mechanism, and the calculated spin-orbit coupling (SOC) values between S_1 and T_1 (gap $\approx$ 0.19 eV) is high enough for intersystem crossing (ISC) to produce efficient triplet excitons for phosphorescence (Fig. S16 in Supporting information).

Compared with high-dimensional scintillators, zero-dimensional (0D) scintillation materials have attracted tremendous attention due to good processibility in flexible scintillation screens, and the homogeneous and small-size microcrystal is beneficial to improve the scintillation screen capability. To unfold the capability of X-ray imaging of Cu_4I_6, the large-area flexible scintillator screen (10×10 cm^2) can be fabricated with soft and deformable PDMS (for details, see Supporting information). As shown in Figs. 4a and b, the processed scintillator screen is characterized by favorable homogeneity and flexibility, and it exhibits uniform green light emission across the entire area under both X-ray and 365 nm UV light excitation and also shows decent transverse tensile property (Fig. S17 in Supporting information). Additionally, we evaluated the X-ray imaging performance of the Cu_4I_6 scintillator screen. As shown in Fig. 4c, the modulation transfer functions (MTF) of X-ray images based on Cu_4I_6 scintillator was obtained. The spatial resolutions is acquired as 12.3 LP/mm where the spatial frequency (LP/mm) at MTF = 0.2, which is superior to some reported perovskite and copper-halide cluster flexible scintillator screens [47,49]. Next, the ballpoint pen and earphones were placed between the cluster scintillation screen and the X-ray source to test the X-ray imaging performance of the actual objects. As shown in Figs. 4d and e, under X-ray irradiation, the metal aperture in the millimeter scale of headset and the spring inside the ballpoint pen can be both clearly observed from X-ray imaging photographs. More importantly, to further evaluate the feasibility of the Cu_4I_6 scintillator screen for dynamic X-ray imaging, the dynamic imaging patterns of a piano metronome were measured. As shown in Fig. 4f, the X-ray imaging patterns of the metronome at different angles of swing can be obviously recorded. In addition, Video S1 (Supporting information) clearly captured the rapid oscillating

behavior of the metronome displayed on the large-area scintillator screen (The video only has noise suppression processing, and the red flash is a small X-ray dose alarm.), under X-ray irradiation. All the above radiation experiments suggest the potential of the Cu_4I_6 scintillator for low-dose healthcare diagnostics and high-quality imaging of static and dynamic objects in practical applications.

In conclusion, an ecofriendly 0D microcrystalline scintillator Cu_4I_6 based on CIEE-active copper iodide cluster was successfully synthesized on a large scale *via* a facile solution method. The Cu_4I_6 cluster shows a high PLQY of 61.23 %, narrowband green emission, large Stokes shifts, and short decay times (as short as 3.59 μs) at room temperature. Compared with the traditional commercial scintillator BGO, uniformly sized Cu_4I_6 microcrystals exhibit high-quality scintillation properties with a low detection limit of 38.4 nGy/s, and high relative light yields of 21,700 photons/MeV. In addition, due to monodispersity of Cu_4I_6 microcrystals, the large-area and flexible X-ray scintillator screen was readily fabricated, which was successfully used for high-resolution imaging on static and dynamic objects, with a spatial resolution of 12.3 lp/mm. We expect that this work can provide a novel tack for preparation of microcrystalline scintillation materials with excellent performance in high-energy detection and X-ray imaging applications.

CRediT authorship contribution statement

Hao-Nan Qin: Writing – original draft, Formal analysis, Data curation. **Hao Xie:** Formal analysis. **Jia-Wang Yuan:** Formal analysis. **Ren-Wu Huang:** Formal analysis, Data curation. **Zhao-Yang Wang:** Writing – review & editing, Supervision, Funding acquisition. **Shuang-Quan Zang:** Writing – review & editing, Supervision, Funding acquisition.

Declaration of competing interest

The authors declare that they have no known competing financial interests or personal relationships that could have appeared to influence the work reported in this paper.

Acknowledgments

This work was supported by the National Natural Science Foundation of China (Nos. 22271258, 92461304) and Henan Province Science and Technology Research and Development Joint Fund (No. 242301420004).

Supplementary materials

Supplementary material associated with this article can be found, in the online version, at doi:10.1016/j.cclet.2025.111529.

References

[1] F. Patat, M. Mapelli, Science 375 (2022) 821–822.
[2] X. Ou, X. Qin, B. Huang, et al., Nature 590 (2021) 410–415.
[3] Q. Chen, J. Wu, X. Ou, et al., Nature 561 (2018) 88–93.
[4] K. Lu, C. He, N. Guo, et al., Nat. Biomed. Eng. 2 (2018) 600–610.
[5] P. Pei, Y. Chen, C. Sun, et al., Nat. Nanotechnol. 16 (2021) 1011–1018.
[6] H. Wu, Y. Ge, G. Niu, J. Tang, Matter 4 (2021) 144–163.
[7] J.D. Valentine, D.K. Wehe, G.F. Knoll, C.E. Moss, IEEE Trans. Nucl. Sci. 40 (1993) 1267–1274.
[8] N. Yasui, Y. Ohashi, T. Kobayashi, T. Den, Adv. Mater. 24 (2012) 5464–5469.
[9] M. Nikl, A. Yoshikawa, Adv. Opt. Mater. 3 (2015) 463–481.
[10] J.D. Valentine, W.W. Moses, S.E. Derenzo, D.K. Wehe, G.F. Knoll, Nucl. Instrum. Methods Phys. Res. Sect. A 325 (1993) 147–157.
[11] W. Li, L. Liu, M. Tan, et al., Adv. Funct. Mater. 31 (2021) 2107843.
[12] Y. Wang, M. Li, Z. Chai, Y. Wang, S. Wang, Angew. Chem. Int. Ed. 62 (2023) e202304638.
[13] S. Shrestha, R. Fischer, G.J. Matt, et al., Nat. Photo. 11 (2017) 436–440.
[14] M. Chen, L. Sun, X. Ou, et al., Adv. Mater. 33 (2021) 2104749.
[15] H. Li, J. Li, N. Shen, et al., Nano Energy 119 (2024) 109055.
[16] E. Auffray, G. Dosovitskiy, A. Fedorov, et al., Phys. Chem. 164 (2019) 108365.
[17] L. Lu, M. Sun, Q. Lu, T. Wu, B. Huang, Nano Energy 79 (2021) 105437.
[18] S. Shrestha, R. Fischer, G.J. Matt, et al., Nat. Photo. 11 (2017) 436–440.
[19] Y.C. Kim, K.H. Kim, D.Y. Son, et al., Nature 550 (2017) 87–91.
[20] X. Li, Y. He, M. Kepenekian, et al., J. Am. Chem. Soc. 142 (2020) 6625–6637.
[21] X. Wang, Y. Wang, Y. Wang, et al., Chem. Commun. 56 (2020) 233–236.
[22] F. Zhang, W. Liang, L. Wang, et al., Adv. Funct. Mater. 31 (2021) 2105771.
[23] Y. Zhang, Y. Fu, X. Song, X. Zhang, Adv. Mater. 34 (2022) 2204710.
[24] M. Gandini, I. Villa, M. Beretta, et al., Nat. Nanotechnol. 15 (2020) 462–468.
[25] H. He, Y. Cui, B. Li, et al., Adv. Mater. 31 (2019) 1806897.
[26] L. Lian, M. Zheng, W. Zhang, et al., Adv. Sci. 7 (2020) 2000195.
[27] X. Wu, Z. Guo, S. Zhu, et al., Adv. Sci. 9 (2022) 2200831.
[28] S. Cho, S. Kim, J. Kim, et al., Light Sci. Appl. 9 (2020) 156.
[29] A. Jana, S. Cho, S.A. Patil, et al., Mater. Today 55 (2022) 110–136.
[30] W. Shao, X. Wang, Z. Zhang, et al., Adv. Opt. Mater. 10 (2022) 2102282.
[31] Q.A. Akkerman, T.P.T. Nguyen, S.C. Boehme, et al., Science 377 (2022) 1406–1412.
[32] Y. Zhang, R. Sun, X. Ou, et al., ACS Nano 13 (2019) 2520–2525.
[33] F. Maddalena, M.E. Witkowski, M. Makowski, et al., ACS Appl. Mater. Interfaces 13 (2021) 59450–59459.
[34] Z. Wang, R. Sun, N. Liu, et al., Nano Res. 15 (2022) 2399–2404.
[35] J.J. Wang, C. Chen, W.G. Chen, et al., J. Am. Chem. Soc. 142 (2020) 3686–3690.
[36] Y. Wang, W. Zhao, Y. Guo, et al., Light Sci. Appl. 12 (2023) 155.
[37] Q.C. Peng, Y.B. Si, J.W. Yuan, et al., Angew. Chem. Int. Ed. 62 (2023) e202308194.
[38] T. He, Y. Zhou, P. Yuan, et al., ACS Energy Lett. 8 (2023) 1362–1370.
[39] J.J. Wang, H.T. Zhou, J.N. Yang, et al., J. Am. Chem. Soc 143 (2021) 10860–10864.
[40] T. Li, Z. Qi, N. Zhang, et al., Adv. Funct. Mater. 34 (2024) 2410361.
[41] T. Chen, S. Yang, J. Chai, et al., Sci. Adv. 3 (2017) e1700956.
[42] M. Yang, X.L. Chen, C.Z. Lu, Dalton Trans. 48 (2019) 10790–10794.
[43] C. Dong, X. Song, B.E. Hasanov, et al., J. Am. Chem. Soc. 146 (2024) 7373–7385.
[44] A.M. Almushaikeh, H. Wang, L. Gutiérrez-Arzaluz, et al., Chem. Commun. 59 (2023) 4447–4450.
[45] Y. Zhou, T. He, P. Yuan, et al., ACS Mater. Lett. 5 (2023) 2002–2008.
[46] P. Yuan, T. He, Y. Zhou, et al., ACS Energy Lett. 8 (2023) 5088–5097.
[47] K. Han, J. Jin, B. Su, J. Qiao, Z. Xia, Adv. Opt. Mater. 10 (2022) 2200865.
[48] Q. Hu, C. Zhang, X. Wu, et al., Angew. Chem. Int. Ed. 62 (2023) e202217784.
[49] F. Zhang, Y. Zhou, Z. Chen, et al., Light Sci. Appl. 17 (2023) 2200848.
[50] H. Li, X. Kang, M. Zhu, Acc. Chem. Res. 57 (2024) 3194–3205.
[51] T. Chen, S. Yang, J. Chai, et al., Sci. Adv. 3 (2017) e1700956.
[52] Y. Zhong, X. Wang, Z. Huang, et al., Nat. Commun. 16 (2025) 2295.
[53] F. Zhang, Y. Zhou, Z. Chen, et al., Adv. Mater 34 (2022) 2204801.